

Chasing Ghosts: A Simulation-to-Real Olfactory Navigation Stack with Optional Vision Augmentation

Kordel K. France

Dept. of Computer Science
University of Texas at Dallas
Richardson, TX, USA
kordel.france@utdallas.edu

Ovidiu Daescu

Dept. of Computer Science
University of Texas at Dallas
Richardson, TX, USA
ovidiu.daescu@utdallas.edu

Latifur Khan

Dept. of Computer Science
University of Texas at Dallas
Richardson, TX, USA
latifur.khan@utdallas.edu

Rohith Peddi

Dept. of Computer Science
University of Texas at Dallas
Richardson, TX, USA
rohith.peddi@utdallas.edu

Abstract—Autonomous odor source localization remains a challenging problem for aerial robots due to turbulent airflow, sparse and delayed sensory signals, and strict payload and compute constraints. While prior unmanned aerial vehicle (UAV)-based olfaction systems have demonstrated gas distribution mapping or reactive plume tracing, they rely on predefined coverage patterns, external infrastructure, or extensive sensing and coordination. In this work, we present a complete, open-source UAV system for online odor source localization using a minimal sensor suite. The system integrates custom olfaction hardware, onboard sensing, and a learning-based navigation policy trained in simulation and deployed on a real quadrotor. Through our minimal framework, the UAV is able to navigate directly toward an odor source without constructing an explicit gas distribution map or relying on external positioning systems. Vision is incorporated as an optional complementary modality to accelerate navigation under certain conditions. We validate the proposed system through real-world flight experiments in a large indoor environment using an ethanol source, demonstrating consistent source-finding behavior under realistic airflow conditions. The primary contribution of this work is a reproducible system and methodological framework for UAV-based olfactory navigation and source finding under minimal sensing assumptions. We elaborate on our hardware design and open source our UAV firmware, simulation code, olfaction-vision dataset, and circuit board to the community.¹

I. INTRODUCTION

How does one find what it cannot see, hear or touch? Navigating by scent has been likened to “chasing ghosts” due to humans’ lack of high bandwidth olfactory perception. Olfaction is the most primitive form of perception, yet artificial intelligence systems have predominantly focused on visual, audio, and linguistic data. This oversight is largely due to the scarcity of olfactory data and the absence of standardized benchmarks, which pose significant challenges for developing and evaluating machine learning models in this domain.

In this study, we introduce a model for olfaction-only navigation, but demonstrate how vision can be complementary to performance. We show how these models can be trained via simulation to run at the edge for scent-based navigation

¹Code, data, and designs available at <https://github.com/KordelFranceTech/ChasingGhosts>

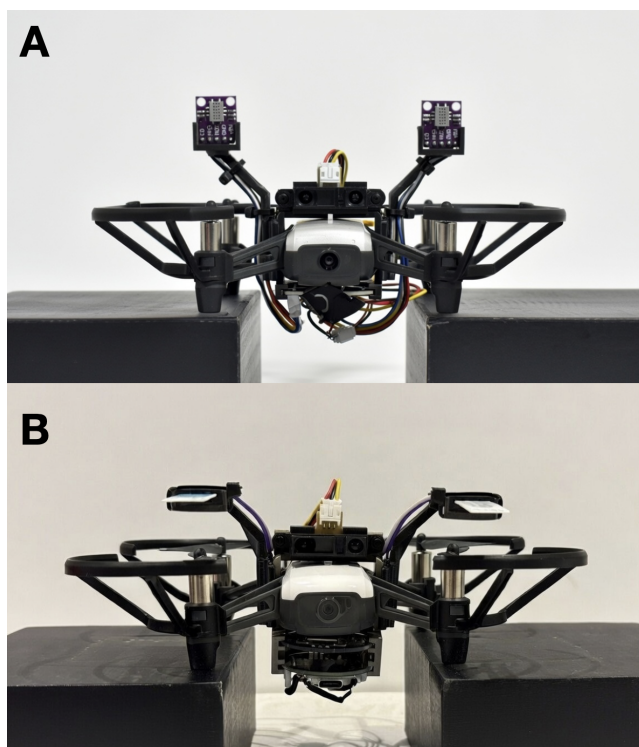


Fig. 1. The UAV equipped with the olfactory processing unit (OPU) and sensor harnesses for scent-based navigation. The metal-oxide sensor configuration is shown in panel A with the electrochemical sensor configuration shown in panel B.

to an odor source. Olfactory navigation is largely absent from robotic functions today, and our motivation for this work is to establish methodology that allow robots to, for example, localize the source of a specified chemical compound, inform automated surgery by mapping olfactory cues to visual components, and inspire alternative forms of underwater navigation via chemical plume tracking. We demonstrate our methodology on a real UAV navigating to a chemical compound.

Due to the hysteresis and non-linearity associated with gas dynamics, navigating by scent is inherently difficult. Current

olfaction sensors suffer from drift and long sampling times [1]–[3] and the inability to accurately perceive the presence of a chemical compound analogizes to “chasing ghosts”. Here, we detail a confluence of adaptive learning techniques, hardware design, sensor selection, and compute optimizations that make this feasible. We provide a detailed account of our hardware, methodologies, and evaluation metrics to ensure transparency and reproducibility. A full bill of materials and code to reproduce our results are detailed in the Supplementary Material. Frontal views of the two configurations used for the UAV are shown in Figure 1.

The contributions of our work are as follows:

- 1) A complete, open-source UAV system for odor source localization, integrating custom olfaction hardware, on-board sensing, simulation, and real-world deployment under payload and compute constraints.
- 2) A learning-based navigation method trained in simulation and deployed on a real UAV, enabling online odor source localization without prior mapping or external positioning infrastructure.
- 3) A minimal-sensor navigation formulation, demonstrating reliable source-seeking behavior using only a small number of olfaction sensors and a single range sensor, with vision used optionally as a complementary modality.
- 4) Real-world experimental validation in a large indoor environment, showing consistent source localization behavior and providing qualitative and quantitative insights into plume navigation under realistic airflow conditions.
- 5) A demonstration that our framework generalizes across sensing mediums.

This work emphasizes system design and methodological integration, on which one could expand with statistically powered evaluation across a wider range of environments and conditions.

II. RELATED WORK

Early UAV-based olfaction systems have focused on gas distribution mapping (GDM), where a predefined flight pattern is used to reconstruct a concentration field and estimate a source location post-hoc. Burgués et al. [4] present a representative example, employing a quadrotor to sample gas concentrations along a sweeping trajectory and infer source location from the reconstructed map. While effective for environmental monitoring, such approaches do not perform online source-seeking behavior and require substantial spatial coverage prior to localization.

Reactive plume tracing methods draw inspiration from biological odor tracking, enabling robots to move toward an odor source based on local concentration cues. Shigaki et al. [5] demonstrate three-dimensional chemical plume tracing using a quadcopter equipped with dual alcohol sensors and onboard ranging, achieving successful localization in controlled indoor environments. Their work highlights the feasibility of UAV-based plume tracking but focuses on reactive control strategies rather than learning-based policies trained across environments.

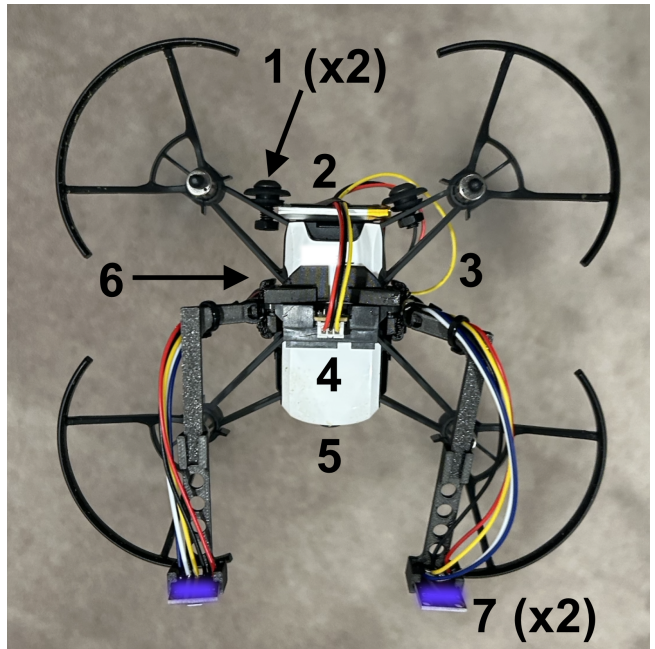


Fig. 2. The UAV equipped with the olfactory processing unit (OPU) and sensor harnesses. The figure shows a top-down view of the aircraft: (1) the 2 ballast points needed to balance the aircraft; (2) the battery to power the motherboard required for the olfactory sensors; (3) the wire harnessing leading to the motherboard attached to the belly of the aircraft; (4) the forward-looking time-of-flight sensor for obstacle avoidance; (5) the forward-looking camera; (6) the motherboard and downward-looking time-of-flight infrared sensors attach to the belly (not shown); (7) the two olfactory sensor antennae (MOX sensors shown, but EC sensors lie at the same location when in the proper configuration).

More recently, learning-based and swarm-based approaches have been explored to improve robustness in turbulent environments. Duisterhof et al. [6] introduce a multi-agent “Sniffy Bug” system that combines bio-inspired navigation with particle swarm optimization, leveraging inter-agent communication and additional sensing modalities. While effective at the swarm level, such systems rely on greater sensing and coordination infrastructure than is available to a single lightweight UAV.

In contrast to prior work, this paper focuses on single-agent, learning-based odor source localization under minimal sensing assumptions. Rather than reconstructing gas distributions or relying on swarm coordination, the proposed system learns a navigation policy in simulation and deploys it directly on a real UAV, enabling online source-seeking behavior in a large indoor environment. The emphasis is on system integration, reproducibility, and sim-to-real transfer, providing a foundation for future statistically powered evaluations and extensions. The works in [4], [6] leverage ultrawide bandwidth (UWB) radio tags placed throughout each course to help the UAV navigate. In contrast, we only allow the UAV to use olfaction (and at the last mile, vision) to guide itself to the odor source and it has no prior knowledge about the course. Unlike the post-mapping over $160m^2$ from [4], we achieve real-time localization over $200m^2$, the largest size experimental course so far, without positional aids.

Work by Hassan, et al. [7] show how robots can navigate by olfactory and visual capabilities, but leverage closed-source online large language models to perform the computation as well as the interpretation of the chemical and vision data, methods impractical for real-time edge robotics. In [4]–[7], the authors use metal oxide sensors as the olfactory receptor. We demonstrate our framework with metal oxide sensors to show improvement on previous work, but also demonstrate that our framework generalizes across sensing mediums with the introduction of electrochemical sensors.

Feng, et al. construct a dataset of vision-olfactory relationships in SmellNet [8], but the dataset is related exclusively to fruits, nuts and other common foods. Ozguroglu, et al. [9] show how vision and olfaction can be linked together through contrastive learning, but the scope is exclusively to botany. We build off many of the methods established by [4], [6], [10]. Namely, we use ethanol as our target compound to maintain parity with their work and provide a level of experimental control.

To the knowledge of the authors, this is the first demonstration of stereo olfactory sensing combined with vision on a UAV over two different chemical sensing mediums. A concise comparison of our work to related work is shown in Section VI-A of the Supplementary Material.

III. METHODS

Our primary goal is to demonstrate that UAVs can navigate purely with olfactory sensors to track a target chemical back to its source. However, we recognize that visual sensors can be complementary to olfactory navigation as seen in several mammals and insects. As a result, we show how understanding the aromas emitted by certain objects can decrease the time needed to localize the target compound through visual confirmation of capturing the odor source.

A. Hardware

We desire a solution for olfactory navigation that is financially and technically accessible to robotics and AI researchers while also reaching the precision required to localize a chemical compound. Therefore, we select off-the-shelf hardware where reasonably possible. Figure 2 shows critical additions to the base UAV airframe, while a full bill of materials is discussed in Section VI-H of the Supplementary Material.

We selected the DJI Tello as the UAV [11], a small open-sourced drone that can be programmed, but contains minimal onboard compute. Unlike prior works [4], [6] that leverage the Crazyflie UAV platform, we require a slightly larger UAV platform with a camera and higher payload that enables us to carry more sensing capability and compute. Three infrared sensors are used for basic stability: two downward-looking sensors for leveling and one forward-looking sensor for obstacle detection. We designed a custom olfactory processing unit (OPU) that contains an ESP-32 microcontroller and a PalmSens EmStat Pico potentiostat attached to the bottom of the UAV. The OPU enables processing of the infrared data for obstacle detection and olfaction sensors to inform navigation,

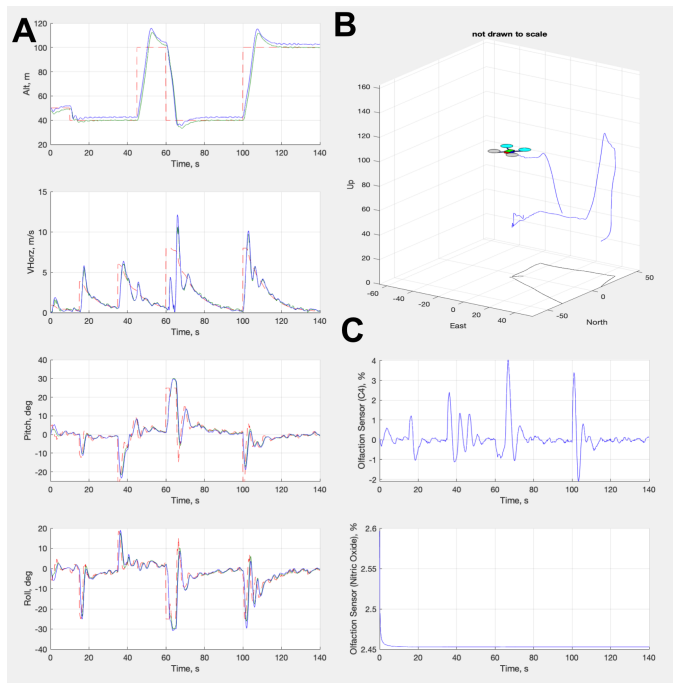


Fig. 3. (A) From top to bottom, this panel shows the altitude, velocity, pitch, and roll from the controller response (blue line) and the command (red line) from the controls algorithms. (B) A diagram showing a partial flight path of the UAV in simulation. (C) From top to bottom, this panel shows the olfactory signal responses for ethanol and nitrogen dioxide.

and wirelessly streams all data back to a laptop ground station for telemetry. We mechanically modify the Tello UAV to accommodate the harnessing, battery, and circuitry needed by the OPU. This required adding 71 grams of ballast to the aft end of the drone in order to counter the forward moment created by the additional components; no additional ballast was needed to adjust for lateral moments. Mechanical brackets and harnessing needed to attach the OPU, olfactory sensors, and infrared sensors to the airframe were designed in SolidWorks [12]. The OPU motherboards were designed using EasyEDA [13]. Details on the electrical and mechanical hardware can be found in Sections VI-G and VI-H, respectively.

B. Simulation

A digital twin of the modified UAV was made for two different simulations. A physics simulation was built via SimuLink to model the control loop algorithms for the UAV, test various flight conditions, and establish a control envelope. A series of plots from this simulation are shown in Figure 3, establishing the performance of the autopilot control algorithms (for more information on these algorithms, see Section 7 and Tables III and IV in the Supplementary Material). This simulation contains a configuration file that enables extrapolation of our control laws to any other UAV platform with our OPU modification. The second simulation was built using Python and the *Gymnasium* framework [14], which we discuss in detail in the next sections. Kalman filters are leveraged and tuned to smooth signals in control responses. Taking inspiration from

olfactory navigation in insects, we position two sensors at the top and fore of the UAV in analogous positions as antennae on the silk moth. This differs from previous approaches of olfactory navigation [4], [6] where the sensor was placed at the top of the body and below the rotors, but is similar to the locations proposed by [5]. Our positioning allows us to perform stereo sensing to ascertain plume direction and avoid volatility from the rotor wash, maximizing the odor signal.

C. Sensors

We desire a generalized solution for olfactory navigation. To aid with down-selection of off-the-shelf olfaction sensors, we designed a small electrical breakout board (see Section VI-G in the Supplementary Material. This allowed us to manually test detection algorithms without having to re-configure the mounting hardware and ballast on the drone. The circuitry and design of this board are available in the repository associated with this paper. The results of the experiments performed with this olfactory board showed that metal oxide (MOX) and electrochemical (EC) were the best for tracking ethanol, and they were selected as the final olfactory effectors as a result.

Metal oxide sensors are rapid in response (1-100 Hz) [15] and are typically sensitive to families of molecules, allowing for more general chemical tracking. We select a pair of Sensirion MICS 6814 sensors due to their prevalence in recent literature [8], [15] and the wide array of compounds they detect. These sensors are sensitive to a variety of gases, but we focus on their sensitivity to ethanol for our work here since ethanol is the target compound.

Metal oxide sensors change resistance based on their exposure to the target gas. This resistance is an indication of gas intensity in the surrounding environment and can be computed according to the following equation:

$$R_s = \left[\frac{V_c}{V_{RL}} - 1 \right] \cdot R_L \quad (1)$$

where R_s indicates the sensor resistance, V_c is the circuit voltage, V_{RL} is the voltage drop over the load resistor, and R_L is the resistance of said load resistor. As Equation 1 is fundamental to the function of the MOX sensor, our optimizations are designed around it. We build off of the methodology from Burgués, et al. in [4] in that we design our algorithm to not be dependent on absolute concentrations in part-per-million or part-per-billion quantity. Rather, we analyze the relative change between time steps of V_{RL} (the temporal difference) and use this to inform the UAV on how to move relative to gas measurements.

Electrochemical sensors are less rapid in response, but much more specific to individual compounds, allowing for more precise tracking. We leverage a two-electrode electrochemical sensor from ItalSens designed to maximize diffusivity of compounds over a certain voltage range for chronoamperometry. Chronoamperometry is the process by which the change in electric current with respect to time over a controlled electrical potential can be measured. This relationship is shown by the Cottrell equation:

$$I = \frac{n_e F A c_k \sqrt{D_k}}{\sqrt{\pi t}} \quad (2)$$

where I denotes the electrical current, measured in amperes; n_e is the number of electrons needed to oxidize one molecule of analyte k ; F is the Faraday constant of 96,485 Coulombs per mol; A denotes the planar area of the electrode in square centimeters; c_k defines the initial concentration of the target analyte k in mols per cubic centimeter; D_k defines the diffusion coefficient for analyte k in square centimeters per second; and t is simply the time the chronoamperometric sequence is running in seconds. Our sensor contains an electrode surface area of 2.25 square centimeters and is specifically tracking a target analyte with a reduction potential of 0.8 V according to Fick’s law. We utilize 1-Ethyl-3-methylimidazolium tetrafluoroborate ($[EMIM][BF_4]$) as the ionic liquid to act as a transducer over our electrodes.

Typically, a single choronamperometric sequence operates anywhere between 6 and 60 seconds. We borrow the method from [3] to infer the analyte diffusion in order to speed up the sampling rate to 0.5-1 Hz. More details on this technique can be found in Section VI-C of the Supplementary Material. Unlike our approach with the MOX sensors, we do adjust the fundamental operation of the EC sensors in Equation 2.

D. Dataset

Pattern recognition over the olfactory data is done via adaptive temporal difference learning. There is no dataset accumulated a priori for training the olfactory sensors as it was determined that adaptively learning the plume via real-time exploration approximation was sufficient, following many of the methods set forth by Sutton in [16]. Data for the olfaction-vision models is sourced from [17] which is a fusion of trusted and peer-reviewed olfactory [18]–[20] and computer vision [21] datasets, and also the only known olfaction-vision dataset.

While modern reasoning models are able to associate from which objects an *aroma* (e.g. lingual descriptors such as "fruity" and "musky") is coming in an image, others find they have difficulty in specifying from where a *chemical compound* (e.g. CO_2 , CH_4) is coming [8], [17], [22]. In addition, leveraging a large vision-language reasoning model - most of which are billions or trillions of parameters in size - is not practical nor necessary for real-time edge robotics. To this end, we construct our own encoder to model olfactory-vision relationships, discussed in Section III-E2.

E. Models

1) *Olfaction-Only Navigation*: To track a plume, we must make some inference on its direction. We use the time-delay estimation between the left and right sensors to inform the horizontal plume angle of attack against the sensor surface. Let x_L and x_R represent the left and right lateral positions of the sensors onboard the aircraft, respectively. For a planar odor front advecting with velocity u , wind speed s , and sensor separation $\Delta x = x_L - x_R$, we can define the expected sensor time constant $\hat{\tau}$ as:

$$\hat{\tau} \approx -\frac{\Delta x \cdot u}{s^2} \quad (3)$$

For a pure lateral baseline Δx and known wind speed s , then the angle ϕ between the plume travel direction and longitudinal axis of the aircraft resolves to:

$$\phi = \arcsin \frac{\hat{\tau} s}{d} \quad (4)$$

This effectively converts a measured time lag into a heading command for the aircraft. We clip ϕ such that $\phi \in [-90, -5] \cup [5, 90]$ such that the UAV will hold the current heading for all $\phi \in (-5, 5)$. Large angles can be likened to casting (exploratory) behaviors in insects, while smaller angles (meaning the UAV stays its current course) can be likened to surging (exploitive) behavior.

The readings are sampled every second from each of the two MOX sensors and every two seconds for the electrochemical sensors. We apply dual-timescale exponential averaging to detect plume bouts while suppressing sensor drift and turbulence noise. This parallels filtering mechanisms observed in insect olfactory neurons. This divergence D is calculated by subtracting a long exponential moving average (EMA) with period β from a short EMA with period α , denoted by E_β and E_α , respectively:

$$D = E_\alpha - E_\beta \quad (5)$$

D can be considered as a temporal-prediction-difference filter, which is mathematically adjacent to TD error computation in reinforcement learning, albeit not a learning mechanism. Although D does not constitute temporal-difference learning in the reinforcement-learning sense, it produces a temporal-prediction error - the difference between fast and slow odor expectations. This is conceptually similar to biological temporal difference filters used in insect olfactory pathways to emphasize odor onset and plume entry events.

We additionally compute a signal line S , which is a smoothed EMA of D with period ρ , where $\alpha < \rho < \beta$. This signal line serves as a dynamic expectation of odor-trend behavior. Positive deviation between lines D and S indicates accelerating odor concentration, consistent with entry into the plume, whereas negative deviation reflects loss of odor momentum and triggers casting behavior. This dual-timescale architecture parallels both biological olfactory adaptation and momentum-based filtering methods in quantitative finance.

Formally, let $C(t)$ define a function over time t for the olfaction sensor readings, where $C_L, C_R \in C$ define functions for the left and right sensors respectively. Then

$$D(t) = E_\alpha(C(t)) - E_\beta(C(t)) \quad (6)$$

And the signal line is

$$S(t) = E_\rho(D(t)) \quad (7)$$

While ϕ gives the UAV the incident angle of the plume against the sensors, the bookkeeping of the D and S sequences allows

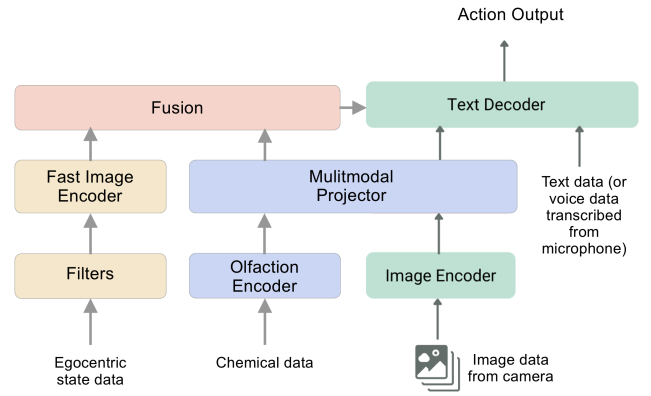


Fig. 4. Olfaction-Vision Model Architecture. Blue and green boxes construct *Component 1* based on *COLIP*. The yellow boxes construct *Component 2*. The output from both models inform reasoning for navigation.

the UAV to determine its proximity relative to the plume. For the experiments shown here, we select empirically deduced values of 3, 8, and 5 for α , β , and ρ , respectively.

2) *Olfaction-Vision Navigation*: For navigation augmented by vision, we train and evaluate a multimodal machine learning model for understanding olfaction-vision relationships. Figure 4 shows the main architecture. It employs a CLIP-based vision encoder [23] to extract visual features from images. A separate 12-layer fully connected encoder processes chemical data from olfactory sensors, converting it into 138-dimension olfactory embeddings. We call this model *COLIP* (*Contrastive Olfaction-Language-Image Pre-training* since it is built on the original CLIP model. A learned linear layer projects both visual and olfactory embeddings into a shared 512-dimension latent space, ensuring compatibility before further processing. A graph associator learns joint relationships between the projected visual and olfactory embeddings. Two such models were evaluated to assess tradeoffs in different architectures: a simple fully-connected network and a graph attention network (GAT). Both models used the same 12-layer encoder. The GAT captured more complex associations between the projected visual and olfactory embeddings, but we found difficulties in reliable performance when exporting to a format that could run at the edge on the UAV. As a result, we do not leverage it for the final analysis because the extra computation and inference time required to run the model would contrast with our desire to run all computation fully at the edge. More details on the training parameters for these models is available in Section VI-D in the Supplementary Material.

Just like its predecessor, *COLIP* undergoes contrastive training using an InfoNCE (Information Noise Contrastive Estimation) loss to align olfactory and visual embeddings, encouraging the model to associate corresponding pairs closely in the latent space. These modality pairs are encoded together, effectively binding them in the process. These encoders are optimized through the InfoNCE loss [24] shown below.

$$L_{I,M} = -\log \frac{\exp(q_i^\top k_i/\tau)}{\exp(q_i^\top k_i/\tau) + \sum_{j \neq i} \exp(q_i^\top k_j/\tau)} \quad (8)$$

where τ denotes a scalar temperature that controls the smoothness of the softmax distribution and j defines "negatives", or unrelated observations. Each example $j \neq i$ in the mini-batch is presumed to be a negative. The loss makes the embeddings q_i and k_i closer in Euclidean distance in joint embedding space. This consequently aligns I with M conveniently for joint learning. A binary classification loss from the graph head is employed to learn relationships between modalities, distinguishing between matching and non-matching olfaction-vision pairs.

Many approaches to robotic control struggle with a core tradeoff: backbones of large vision models are highly general but too slow for real-time operation, while traditional robot visuomotor policies are fast but lack generalization [25]. We resolve this tradeoff by introducing a dual-system architecture. Component 1 is the OVM that runs at 0.1-0.2 Hz. It is responsible for high-level scene understanding and multi-modal comprehension, enabling broad generalization across objects, environments, and goals. Component 2, is a high-speed reactive vision-olfaction module containing a fine-tuned YOLOv11 [26] for rapid vision inference running inference at 1-2 Hz. Component 1 is mainly used in confirming whether the acceptance criteria for locating the odor source have been achieved (see Section III-H for more on this). Component 2 is designed to synchronize at the same sampling rate as the olfaction sensors, and helps convert the latent representations from the OVM into precise, continuous UAV actions.

This decoupled design lets each component function at its optimal temporal scale. Component 2 can deliberate slowly over abstract goals, while Component 1 executes rapid, low-latency commands in response to dynamic conditions. This relieves the need to model increased complexity in our plume models and simulations. Furthermore, the separation of both components allows for independent development and iteration.

F. Navigation & Plume Models

Plume models are inherently complex and require advanced computational fluid dynamics engines to achieve reasonable approximations. We seek a set of algorithms that generalize well to all chemical compounds and follow simple rules based on environmental evidence, not unlike those followed by insects [10], [27], [28]. The primary navigation model was a simple bout detection algorithms [6], [29] leveraging the first and second derivatives are aligned with short and long moving averages of the olfactory signal coupled with inertial data to determine the UAV actions. For brevity, we denote this model as *olfactory inertial odometry (OIO)* building off the principles from [30]. Plumes are modeled with simple Gaussian time-series processes with blanks [31] inserted into the data to resemble wind shifts and plume volatility. The robot is allowed seven actions depending on temporal plume dynamics: surge forward, cast in one of four directions, pause,

or land. A selection of the "land" action indicates that the UAV is confident it has found the plume source. Our perception reasoning is highly susceptible to hysteresis due to the ability of shifting plume dynamics. Tuned Kalman filters and sensor synchronization are employed to counter this. A custom plume environment was implemented using the *Gymnasium* framework [14] for additional simulations in plume tracking. Factors such temperature, relative humidity, barometric pressure, wind direction, wind magnitude, wind sparsity, and air chemical composition were all designed to be tunable hyperparameters of the plume. The design follows Gaussian plume principles [28] and a Dryden turbulence model [32]. More details about this plume environment and its construction can be found in Section VI-F of the supplementary material.

A second navigation model based on reinforcement learning (RL) was implemented to provide a more comprehensive assessment of the navigation. *Q-learning* [33] is a standard temporal difference RL algorithm used in many applications. Due to the dynamism of plumes and the UAV's frequent probability to travel off plume, we employ eligibility traces to harmonize immediate and long-term rewards. *TD*(λ) algorithms leverage eligibility traces to give credit to more recent λ states instead of only the current state ($\lambda = 0$). Consequently, we leverage the *TD*(λ) derivatives of *Q-learning* and Expected SARSA, called *Q*(λ) and *Expected SARSA*(λ), respectively [34]. While both models are trained in simulation, we found Expected SARSA (λ) to be the model most robust to reasoning about blank pockets of air, and thus selected it as a finalist for evaluation in our experiments. Expected SARSA(λ) proved most robust for air with continuous gradients, but this scenario is not practical for real world applications. Exact training parameters for these models can be found in the Supplementary Material in Section VI-E.

With either model, we discretize the aircraft's movements such that it is only allowed to move 30 cm at each time step. We find that making the actions continuous was not necessary as doing so added more complexity to our simulations and did not substantially improve them. In addition, the infrared sensors enable the UAV to make a decision on how to move forward. We acknowledge that enabling continuous action spaces could be an opportunity for future work.

G. Course

Finally, we transfer our solution to the real world with flight tests on the UAV. Our UAV is deployed over a 200 m^2 course, depicted in Figure 5. We start by placing 100 mL of ethanol within a home diffuser in Room 2 as indicated by the checkered flag. The diffuser diffuses the ethanol at a rate of 2.16 mL per minute. The diffuser is placed near an 80-cm home fan that exhausts air at 1415 liters per minute in order to develop a small plume for traceability of the compound. The robot starts at the far adjacent end of the map as indicated by the UAV icon in the figure. We observe 5 runs each with the target compound lying in both rooms 1 and 2. At the beginning of each run, the compound is given 5 minutes to disperse and form the start of a plume before

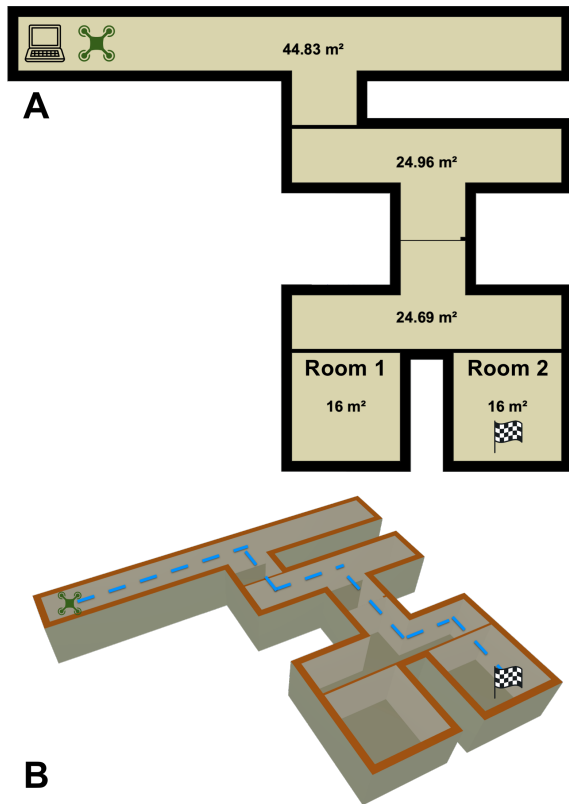


Fig. 5. Illustration of the course developed for olfactory navigation by the UAV. Figure A shows a bird’s-eye-view of the course, where the ground station (laptop icon) is located at the top left and the UAV (quadcopter icon) takes off next to it; Room 2 hosts the target compound and the plume is formed from here. Figure B shows an isometric view of the ideal path the UAV should pursue to locate the source.

the UAV is commanded for takeoff. After takeoff is initiated, there is no human intervention with the UAV until it sends a response back to the ground station that the source of the target compound has been found. Between each run, the course is vented and air measurements are taken to ensure that the next iteration may begin with a clean baseline and to encourage as reproducible results as possible. Due to the length of time needed to properly vent the course, the uncontrollable HVAC schedules within the test building, and other experimental controls needed to re-initialize to a stable environment, the number of statistical runs we can perform is limited. As a result, for each of the four tasks, we analyze five trials. We note that prior work from [4] and [6] have a low count of statistical runs (identical to ours) also suspected by these factors.

H. Task Termination Criteria

One defining contribution of our work is how a UAV decides it is “done”. For the robot to determine whether it has found the source of the gas, it must evaluate a hypothesis about whether it believes it has found the highest concentration of the plume given its observed samples. On our selected UAV, the IMU bias from the added payload was significant, making long-term positional estimation very difficult. See Figure 6

as an example of the IMU replay that occurred over the map detailed in Figure 5. Short-term estimation was filtered accordingly for reasoning via OIO.

To evaluate when the UAV has reached the gas source we construct a minimum-variance unbiased point estimator \hat{C} to approximate the true highest concentration of the gas within the environment, given by:

$$\hat{C} = m \frac{k}{k+1} - 1 \quad (9)$$

where m is the largest concentration observed by the olfaction sensors and k is the total number of samples observed. We assume that once a chemical packet has been observed, it can be observable again, as in drawing with replacement [35], [36].

The point estimate becomes reliable only after long sessions with several observed samples. However, because we desire a generalized solution to both short and long exploration sessions, we compute a confidence interval for \hat{C} . We compute the p -th and q -th quantiles of the sample maximum m to form the interval $[\hat{C}q^{1/k}, \hat{C}p^{1/k}]$ which yields the corresponding confidence interval for the maximum estimated gas source concentration over the full population of gas samples:

$$\left[\frac{m}{q^{1/k}}, \frac{m}{p^{1/k}} \right] \quad (10)$$

As an example, assume the UAV has observed 20 samples and believes that it has found the source of the gas with an observed final concentration m . The point estimate for $k = 20$ samples would be $1.05m$ based on Equation 9. By Equation 10, taking a 95% confidence interval would return

$$\left[\frac{m}{0.975^{1/20}}, \frac{m}{0.025^{1/20}} \right] = [1.001m, 1.2025m] \approx [m, 1.2m] \quad (11)$$

This indicates that, given the observed plume concentrations, we can be 95% confident that the true highest concentration of the plume lies between the current observed highest concentration m and a concentration 20% larger. From here, the UAV can determine whether to keep navigating or to end. In general, we strive to be within 25% of the expected maximum odor concentration based on a 95% confidence interval; so in this case, the UAV would land and stop navigating.

IV. RESULTS

Final results for our experiments are shown in Table I. For all trials, the UAV successfully found the source of the target compound, which was our minimum bar for success. We observe that electrochemical-based olfactory sensors require more time to complete the task in general, and we suspect this is due to the fact that EC sensors are designed to be more sensitive to perturbations in the target compound’s concentration which could cause them to overfit to noise or small eddy currents in the plume. For both MOX and EC sensors, we note a small bump in performance by adding vision as a modality by which to localize the odor. In all tasks, the UAV only uses olfaction to navigate. In the *Olfaction*

TABLE I
FINAL RESULTS

Method	Sensor Type	Nav. Algorithm	Average Time μ_t (s)	Sigma Time, σ_t (s)	Best Time, β_t (s)
Olfaction	MOX	OIO	98.38	14.84	71.59
Olfaction	EC	OIO	112.22	16.70	97.65
Olfaction	MOX	E.SARSA(λ)	103.99	14.89	82.73
Olfaction	EC	E.SARSA(λ)	121.85	16.77	97.10
Olfaction + Vision	MOX	OIO	94.03	14.68	66.12
Olfaction + Vision	EC	OIO	107.71	17.07	80.50

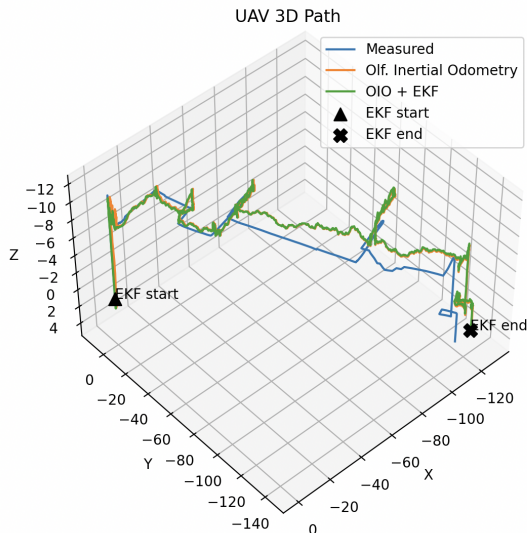


Fig. 6. The IMU replay of the UAV traveling over the whole course is shown here. Unfiltered olfactory inertial odometry (OIO) [30], [37] along with filtered OIO via EKF are shown alongside naked measurements from the IMU. The addition of the olfaction sensors and OPU as payload significantly biased the IMU. This made compound mapping via long-term inertial odometry nearly impossible and drove our decision for the task termination criteria in Section III-H. Measurements are in centimeters.

+ *Vision* tasks, the UAV only activates the camera when it cannot maximize the olfactory gradient any more, which usually occurs when the UAV is confident it has reached the target compound based on the termination criteria. When only olfaction is used, we observed that the UAV would spend several seconds slowly moving around the chemical source, trying to maximize the olfactory signal. Because diffusion of the gas is more uniform the closer one is to the gas’s source, an apparent gradient may not be easy to determine, and the UAV will waste several seconds moving around very close to the source. This is where vision became additive: using a visual confirmation that the source had been found allows the UAV to not waste time and battery chasing small gradients. As a consequence, vision shortened navigation times by shaving a few seconds off the end of each trial, where olfaction-only navigation would have kept the UAV flying.

V. DISCUSSION & LIMITATIONS

The most important conclusion drawn from our experiments was that olfaction is enough to navigate when localizing

to an odor source. We believe this is the first documented attempt to enable a robot to navigate purely by scent without any planning, a priori knowledge of the environment, or location aids such as UWB radio tags. We attempt to show our results generalize by performing experiments with two different olfaction sensor types. However, we acknowledge that there is a larger variety of chemical sensors that exist. In addition, our work here is performed over only one chemical compound: ethanol. This is intentional in order to build off of the assumptions and work by Burgues, et al. [4] and Duisterhof, et al. [6], as they demonstrate olfactory navigation with radio tags and metal oxide sensors in tracking ethanol. We note that our results show that the UAV localized itself to the chemical source on *every* trial, while the work of Shigaki, et al. [5] noted a non-perfect localization rate. Work to demonstrate the generalization of our framework over other environments, chemical compounds, and sensor types such as graphene-based sensors, spectroscopy sensors, and photo-ionization detectors is ongoing. We acknowledge that exact replication of any olfactory navigation task is difficult due to the inherent non-linearities of gas dynamics and the difficulty in replicating exact initial chemistry conditions. As a result, the focus of our work here is to establish a simple, reproducible, and generalized framework on which other researchers can build to conduct additional experiments that lead to further improvements and increased reproducibility.

VI. CONCLUSION

Scent-based navigation is a very nuanced robotics task. Organisms that leverage olfaction to perceive the world optimize over various criteria, yet none of them are standardized. With our framework and experiments here, we show that, to localize a UAV to a chemical source, olfactory perception is enough. We incorporate many nature-inspired principles to define methods for the first instance of stereo olfaction-vision odor localization and demonstrate their practicality with real aerial robots. Our code, simulations, hardware schematics, and datasets are made available to the community to encourage advancement in the field. We hope the techniques presented here encourage more work in olfactory robotics and bring us one step closer to enabling the sense of smell for machines.

REFERENCES

- [1] N. Dennler, S. Rastogi, J. Fonollosa, A. van Schaik, and M. Schmukeyer, “Drift in a popular metal oxide sensor dataset reveals limitations for gas classification benchmarks,” *Sensors and Actuators B:*

- Chemical*, vol. 361, p. 131668, 2022. [Online]. Available: <https://www.sciencedirect.com/science/article/pii/S0925400522003100>
- [2] N. Dennler, A. van Schaik, and M. Schmuker, "Limitations in odour recognition and generalization in a neuromorphic olfactory circuit," *Nature Machine Intelligence*, vol. 6, pp. 1451–1453, 2024.
 - [3] K. K. France, "Chronoamperometry with room-temperature ionic liquids: Sub-second inference techniques," 2025. [Online]. Available: <https://arxiv.org/abs/2506.04540>
 - [4] J. Burgués, V. Hernández, A. J. Lilienthal, and S. Marco, "Smelling nano aerial vehicle for gas source localization and mapping," *Sensors*, vol. 19, no. 3, 2019. [Online]. Available: <https://www.mdpi.com/1424-8220/19/3/478>
 - [5] S. Shigaki, M. R. Fikri, and D. Kurabayashi, "Design and experimental evaluation of an odor sensing method for a pocket-sized quadcopter," *Sensors*, vol. 18, no. 11, 2018. [Online]. Available: <https://www.mdpi.com/1424-8220/18/11/3720>
 - [6] B. P. Duisterhof, S. Li, J. Burgués, V. J. Reddi, and G. C. H. E. de Croon, "Sniffy bug: A fully autonomous swarm of gas-seeking nano quadcopters in cluttered environments," in *2021 IEEE/RSJ International Conference on Intelligent Robots and Systems (IROS)*, 2021, pp. 9099–9106.
 - [7] S. Hassan, L. Wang, and K. R. Mahmud, "Robotic odor source localization via vision and olfaction fusion navigation algorithm," *Sensors*, vol. 24, no. 7, 2024. [Online]. Available: <https://www.mdpi.com/1424-8220/24/7/2309>
 - [8] D. Feng, C. Li, W. Dai, and P. P. Liang, "Smellnet: A large-scale dataset for real-world smell recognition," 2025. [Online]. Available: <https://arxiv.org/abs/2506.00239>
 - [9] E. Ozguroglu, J. Liang, R. Liu, M. Chiquier, M. DeTienne, W. W. Qian, A. Horowitz, A. Owens, and C. Vondrick, "New york smells: A large multimodal dataset for olfaction," 2025. [Online]. Available: <https://arxiv.org/abs/2511.20544>
 - [10] S. H. Singh, F. van Breugel, R. P. N. Rao, and B. W. Brunton, "Emergent behaviour and neural dynamics in artificial agents tracking odour plumes," *Nature Machine Intelligence*, vol. 5, no. 1, pp. 58–70, Jan 2023. [Online]. Available: <https://doi.org/10.1038/s42256-022-00599-w>
 - [11] D. F. Escoté, "DJITelloPy: Python library to interact with the DJI Tello drone," <https://github.com/damiafuentes/DJITelloPy>, 2019, accessed: 2025-07-23. [Online]. Available: <https://github.com/damiafuentes/DJITelloPy>
 - [12] D. Systèmes, "Solidworks," computer-Aided Design (CAD) Software. [Online]. Available: <https://www.solidworks.com>
 - [13] J. . LCSC, "Easyeda - online pcb design tool," <https://easyeda.com/>, 2024-2025, accessed: 2026-01-19.
 - [14] G. Brockman, V. Cheung, L. Petterson, J. Schneider, J. Schulman, J. Tang, and W. Zaremba, "Openai gym," *CoRR*, vol. abs/1606.01540, 2016. [Online]. Available: <http://arxiv.org/abs/1606.01540>
 - [15] N. Dennler, D. Drix, T. P. Warner, S. Rastogi, C. D. Casa, T. Ackels, A. T. Schaefer, A. van Schaik, and M. Schmuker, "High-speed odor sensing using miniaturized electronic nose," *Science Advances*, vol. 10, no. 45, p. eadp1764, 2024.
 - [16] R. S. Sutton, "Learning to predict by the methods of temporal differences," *Mach. Learn.*, vol. 3, no. 1, p. 9–44, Aug. 1988. [Online]. Available: <https://doi.org/10.1023/A:1022633531479>
 - [17] K. K. France and O. Daescu, "Diffusion graph neural networks and dataset for robust olfactory navigation in hazard robotics," 2025. [Online]. Available: <https://arxiv.org/abs/2506.00455v3>
 - [18] T. G. S. Company, "The good scents company information system," <http://www.thegoodscentscompany.com/>, accessed: 2025-03-08.
 - [19] L. . Associates, "Pmp 2001 - database of perfumery materials and performance," <http://www.leffingwell.com/bacispmp.htm>, accessed: 2025-03-08.
 - [20] B. K. Lee, E. J. Mayhew, B. Sanchez-Lengeling, J. N. Wei, W. W. Qian, K. A. Little, M. Andres, B. B. Nguyen, T. Moloy, J. Yasonik, J. K. Parker, R. C. Gerkin, J. D. Mainland, and A. B. Wiltchko, "A principal odor map unifies diverse tasks in olfactory perception," *Science*, vol. 381, no. 6661, pp. 999–1006, 2023. [Online]. Available: <https://www.science.org/doi/abs/10.1126/science.ade4401>
 - [21] T. Lin, M. Maire, S. J. Belongie, L. D. Bourdev, R. B. Girshick, J. Hays, P. Perona, D. Ramanan, P. Dollár, and C. L. Zitnick, "Microsoft COCO: common objects in context," *CoRR*, vol. abs/1405.0312, 2014. [Online]. Available: <http://arxiv.org/abs/1405.0312>
 - [22] S. Zhong, Z. Zhou, C. Dawes, G. Brianz, and M. Obrist, "Sniff ai: Is my 'spicy' your 'spicy'? exploring llm's perceptual alignment with human smell experiences," 2024. [Online]. Available: <https://arxiv.org/abs/2411.06950>
 - [23] X. Zhai, B. Mustafa, A. Kolesnikov, and L. Beyer, "Sigmoid loss for language image pre-training," 2023. [Online]. Available: <https://arxiv.org/abs/2303.15343>
 - [24] A. van den Oord, Y. Li, and O. Vinyals, "Representation learning with contrastive predictive coding," 2019.
 - [25] J. Eschmann, D. Albani, and G. Loianno, "Learning to fly in seconds," *IEEE Robotics and Automation Letters*, vol. 9, no. 7, pp. 6336–6343, 2024.
 - [26] R. Khanam and M. Hussain, "Yolov11: An overview of the key architectural enhancements," 2024. [Online]. Available: <https://arxiv.org/abs/2410.17725>
 - [27] G. Singh, D. Lofaro, and D. Sofge, "Pursuit-evasion with decentralized robotic swarm in continuous state space and action space via deep reinforcement learning," in *Proceedings of the 12th International Conference on Agents and Artificial Intelligence - Volume 1: ICAART, INSTICC*. SciTePress, 2020, pp. 226–233.
 - [28] J. Crimaldi, H. Lei, A. Schaefer, M. Schmuker, B. H. Smith, A. C. True, J. V. Verhagen, and J. D. Victor, "Active sensing in a dynamic olfactory world," *Journal of Computational Neuroscience*, vol. 50, no. 1, pp. 1–6, Feb 2022. [Online]. Available: <https://doi.org/10.1007/s10827-021-00798-1>
 - [29] M. Schmuker, V. Bahr, and R. Huerta, "Exploiting plume structure to decode gas source distance using metal-oxide gas sensors," *Sensors and Actuators B: Chemical*, vol. 235, pp. 636–646, 2016. [Online]. Available: <https://www.sciencedirect.com/science/article/pii/S0925400516307833>
 - [30] K. K. France, O. Daescu, A. Paul, and S. Prasad, "Olfactory inertial odometry: Sensor calibration and drift compensation," 2025. [Online]. Available: <https://arxiv.org/abs/2506.04539>
 - [31] N. Dennler, A. True, A. van Schaik, and M. Schmuker, "Neuromorphic principles for machine olfaction," *Neuromorphic Computing and Engineering*, vol. 5, no. 2, p. 023001, may 2025. [Online]. Available: <https://dx.doi.org/10.1088/2634-4386/add0dc>
 - [32] H. W. LIEPMANN, "On the application of statistical concepts to the buffeting problem," *Journal of the Aeronautical Sciences*, vol. 19, no. 12, pp. 793–800, 1952. [Online]. Available: <https://doi.org/10.2514/8.2491>
 - [33] C. Watkins, "Learning from delayed rewards," Ph.D. dissertation, Department of Computer Science, Kings College, Cambridge University, 1989.
 - [34] R. S. Sutton and A. G. Barto, *Reinforcement Learning: An Introduction*. MIT Press, 2018.
 - [35] G. Clark, A. Gonye, and S. J. Miller, "Lessons from the german tank problem," 2021. [Online]. Available: <https://arxiv.org/abs/2101.08162>
 - [36] C. M. Simon, "A bayesian treatment of the german tank problem," *The Mathematical Intelligencer*, vol. 46, no. 2, pp. 117–127, Jun 2024. [Online]. Available: <https://doi.org/10.1007/s00283-023-10274-6>
 - [37] K. K. France, O. Daescu, A. Paul, and S. Prasad, "Olfactory inertial odometry: Sensor calibration and drift compensation," 2025. [Online]. Available: <https://arxiv.org/abs/2506.04539>
 - [38] I. Goodfellow, Y. Bengio, and A. Courville, *Deep Learning*. MIT Press, 2016. <http://www.deeplearningbook.org>.
 - [39] K. K. France and O. Daescu, "Diffusion graph neural networks and dataset for robust olfactory navigation in hazard robotics," 2025. [Online]. Available: <https://arxiv.org/abs/2506.00455v3>
 - [40] K. K. France, "Scientece-ovlc-v1: Joint olfaction-vision-language classifiers," Hugging Face, 2025. [Online]. Available: <https://huggingface.co/kordelfrance/Olfaction-Vision-Language-Classifiers>
 - [41] R. S. Sutton and A. G. Barto, *Reinforcement Learning: An Introduction*, 2nd ed. The MIT Press, 2018.
 - [42] K. K. France and J. W. Sheppard, "Factored particle swarm optimization for policy co-training in reinforcement learning," in *Proceedings of the Genetic and Evolutionary Computation Conference*, ser. GECCO '23. New York, NY, USA: Association for Computing Machinery, 2023, p. 30–38. [Online]. Available: <https://doi.org/10.1145/3583131.3590376>
 - [43] K. K. France, A. Paul, I. Banga, and S. Prasad, "Emergent behavior in evolutionary swarms for machine olfaction," in *Proceedings of the Genetic and Evolutionary Computation Conference*, ser. GECCO '24. New York, NY, USA: Association for Computing Machinery, 2024, p. 30–38. [Online]. Available: <https://doi.org/10.1145/3583131.3590376>
 - [44] Scientece, "Scientece app: Olfactory interface instrument," 2025, accessed: 2025-03-02. [Online]. Available: <https://scientece.ai/news/!scientece-app-worlds-first-olfaction-vision-language-model>

SUPPLEMENTARY MATERIAL

A. Overview of Related Work

A high-level comparison of our work presented here to previous research in olfaction navigation. We strived to maintain parity with existing research and build off of their assumptions and methods for a level of experimental control while integrating our own optimizations. These papers are the closest we found to our research.

TABLE II: Comparison to Relevant Prior Works

Aspect	Shigaki et al. (2018/2023 variants)	Burgués et al. (2019)	Duisterhof et al. (2021)	Our Work
Robot Type	Pocket-sized quadcopter (2018) or ground crawler (2023); single unit.	Nano quadcopter (Crazyflie).	Swarm of nano quadcopters (Crazyflie).	Modified DJI Tello UAV; single unit but with custom harness for stereo sensors. Larger payload for dual sensors and vision integration.
Sensors	Single MOX sensor (2018) or dual alcohol + wind sensors (2023).	Single MOX (TGS 8100).	Single MOX per drone + laser rangers.	Dual MOX/EC sensors in stereo (antennae-like); IR for obstacles; vision complementary. First stereo olfaction demo; multiple sensor types for generalization.
Navigation Approach	Bio-inspired (surge-cast/zigzag); real-time with odor frequency.	Predefined sweeping path; bout detection or concentration mapping.	Mapless bug algorithm with PSO; real-time swarming.	Adaptive TD learning (OIO/Q(λ)); real-time plume modeling with temporal differences. TD(λ) for plumes; no a priori path; vision for "last-mile" confirmation.
Course Size	Small (1.5-2m start distance; indoor/outdoor open areas).	160m ² indoor.	10x10m (100m ²) with obstacles.	200m ² indoor with rooms. Largest course; more complex (multi-room plume dynamics).
Success Rate	80-90% (2018: non-perfect; 2023: high but variable in complex envs).	N/A (mapping error 1-2m; not framed as success rate).	92% in sim; 11/12 real runs.	100% across 20+ trials. Perfect localization; robust to hysteresis without overfitting.
Real-Time vs. Post-Mapping	Real-time (autonomous onboard).	Post-mapping (builds 3D map after flight; potential for real-time discussed but not implemented).	Real-time (mapless, autonomous).	Real-time (edge-only; no post-analysis). True real-time source localization (not just mapping like Burgués); straight to source.
Positioning Aids	None (onboard only).	External UWB anchors for 3D positioning.	Onboard UWB for relative localization.	None (only onboard IR + olfaction; naive to environment). Fully aid-free; no UWB/radio tags like Burgués/Duisterhof.
Other	Focus on bio-mimicry; ethanol source.	Gas mapping; ethanol.	Swarm coordination; sim-to-real.	Olfaction-vision models; custom hardware; open source. Vision augmentation; edge ML; sim plume env.

B. Control Algorithms

The autopilot control loop was based on a *Proportional-Integral Controller with Rate Feedback*, or *PIR* for short. The control diagram is shown below in Figure 7. Explanations of each parameter are shown in Table III. The values for each gain of each controller are shown in Table IV.

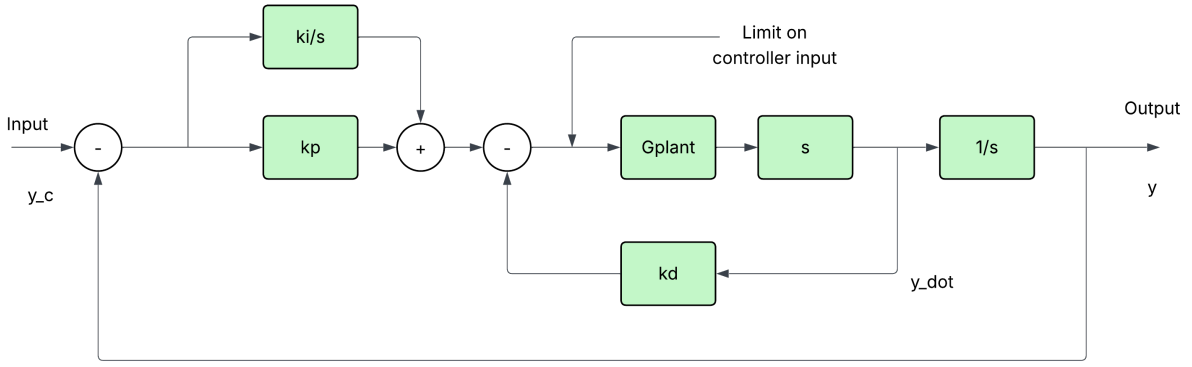


Fig. 7. The control loop was designed to model the DJI Tello control algorithms and understand how to sequence the olfaction sensors with the other sensors.

TABLE III
PI CONTROLLER WITH RATE FEEDBACK

Parameter	Definition
G_{plant}	Controller
y_c	Closed loop command
y	Current system response
\dot{y}	Rate feedback
dt	timestep, in seconds
k_i	integral gain
k_p	proportional gain
k_d	derivative gain

TABLE IV
PID GAINS FOR EACH PIR CONTROLLER

Parameter	Value
k_p (roll)	0.010
k_i (roll)	0.002
k_d (roll)	0.006
k_p (altitude)	0.070
k_i (altitude)	0.015
k_d (altitude)	0.060-0.080
k_p (pitch)	0.010-0.012
k_i (pitch)	0.002
k_d (pitch)	0.010
k_p (yaw)	0.100-0.200
k_i (yaw)	0.012
k_d (yaw)	0.100
k_p (velocity lateral)	0.100
k_i (velocity lateral)	0.050
k_d (velocity lateral)	0.000-0.010
k_p (velocity longitudinal)	0.100
k_i (velocity longitudinal)	0.050
k_d (velocity longitudinal)	0.000-0.010

C. Inference Technique for Electrochemical Sensors

For metal oxide sensor measurement, principles from Dennler, et al. in [15] are used. For measurements with electrochemical sensors, we borrow the fast inference technique for chronoamperometry from [3]. We evaluate two sampling rates for chronoamperometry: 10 Hz and 100 Hz. It was determined that, while 10 hz was computationally cheaper, 100 Hz gave us more points from which the fast inference algorithm can infer, so we set 100 Hz as the sampling rate for deployment on the UAV and cut the chronoamperometry measurement after 1.0 second. Plots for assessing how well the inference technique predicted the full 6-second diffusion sequence is shown in Figure 8 for a 100-Hz measurement frequency and in Figure 9 for a 10-Hz measurement frequency.

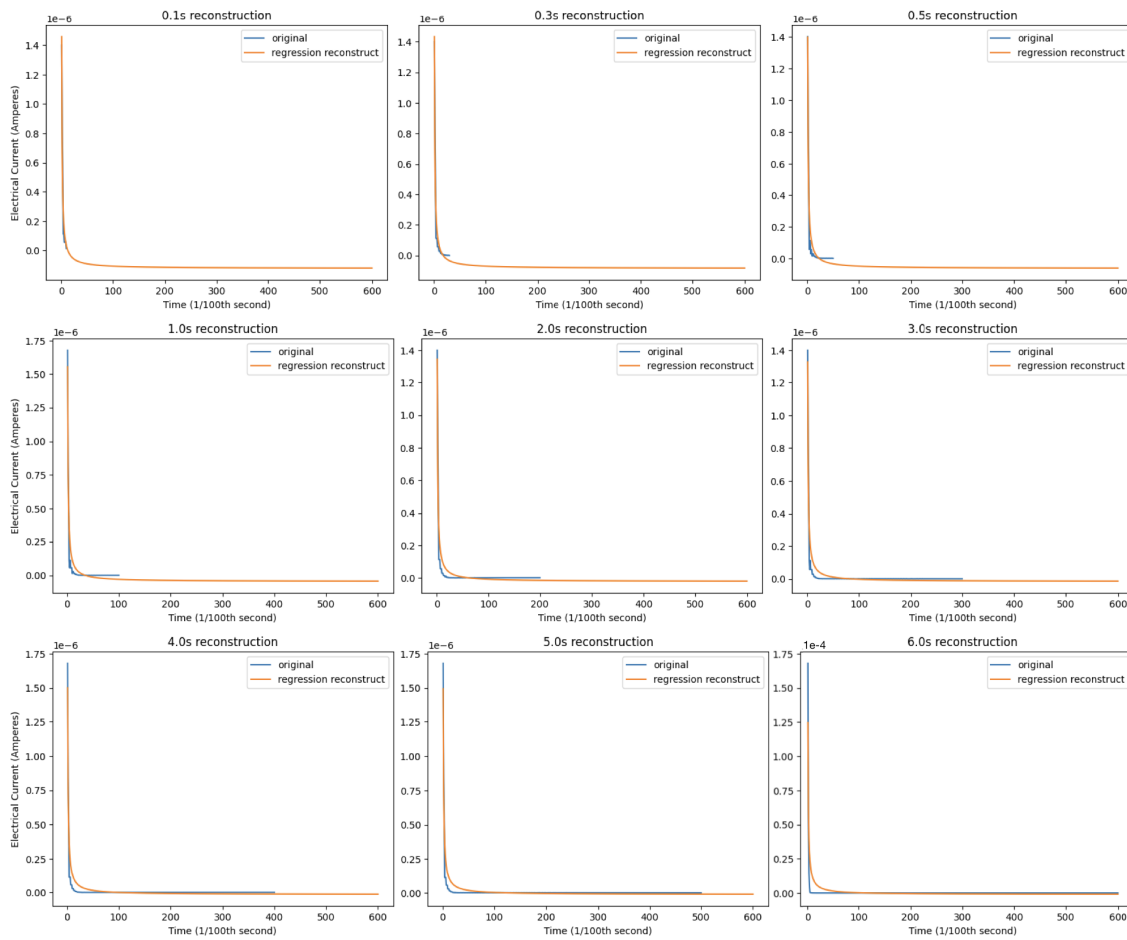


Fig. 8. Prediction of the full 6-second diffusion current for chronoamperometry over various time periods at a 100-Hz measurement frequency.

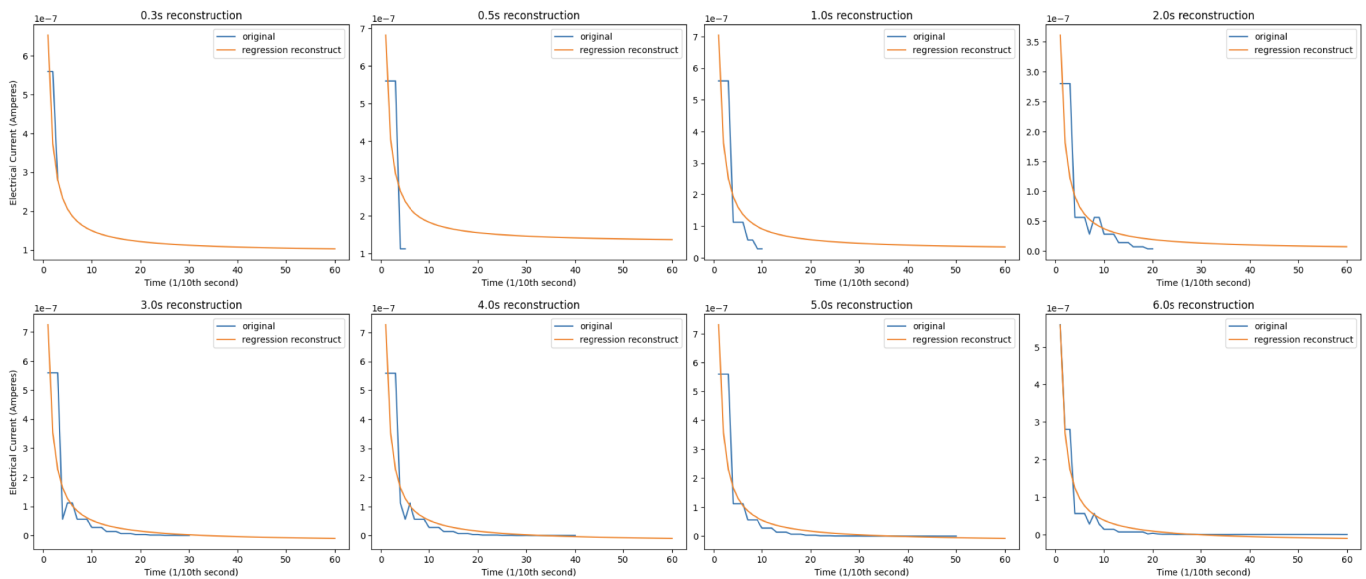


Fig. 9. Prediction of the full 6-second diffusion current for chronoamperometry over various time periods at a 10-Hz measurement frequency.

D. Training of Olfaction-Vision Models

An encoder was trained to compress olfactory data into a format that could be jointly learned with CLIP through a graph associator model. We intentionally kept this encoder simple in architecture due to issues in exporting advanced layers that we observed with the graph associator models (more on this below). The encoder is a very deep model, but we intentionally over-parameterized it due to the low additional computational overhead and because there is a general lack of open-sourced olfactory training data from which to learn (depth and over-parameterization has been shown to help models generalize in the absence of plentiful data [38]). Details on encoder training can be found below:

TABLE V
OLFACTION ENCODER

Parameter	Value
layers	12
layer types	Fully connected only
input dimension	138
output dimension	512
batch size	16
learning rate	1e-4
activation functions	ReLU
epochs	1100
loss function	Information noise-contrastive estimation
loss function temperature	0.07
optimizer	Adam

Two graph associator machine learning models were trained to learn olfaction-vision relationships: a fully-connected (FC) neural network and a graph-attention (GAT) neural network. The simple FC network was optimized to export for use at the edge without external API calls. This model contains lower computational demand, lower layer complexity (and thus easier exportability), and faster inference. Details on its architecture are shown below:

TABLE VI
FC GRAPH ASSOCIATOR

Parameter	Value
layers	4
layer types	Fully connected only
input dimension	512
output dimension	512
embedding dimension	512
batch size	16
learning rate	1e-4
activation functions	ReLU
epochs	1100
loss function	Information noise-contrastive estimation
loss function temperature	0.07
optimizer	Adam

The GAT associator learned more complex relationships between CLIP and olfactory representations. However, we noted a lack of consistency in inference performance between what was observed when training the models and what was actually observed when exported to the UAV firmware. As a result, we did not move forward with this architecture as the baseline model. Details on GAT training are shown below:

TABLE VII
GAT GRAPH ASSOCIATOR

Parameter	Value
layers	4
layer types	2 fully connected, 2 GAT Convolution
input dimension	512
output dimension	512
embedding dimension	512
batch size	16
learning rate	1e-4
activation functions	ReLU
epochs	1100
loss function	Information noise-contrastive estimation
loss function temperature	0.07
optimizer	Adam

The loss plot of the final training run for both graph associator models jointly trained with the olfactory encoder + CLIP are shown below in Figure 10.

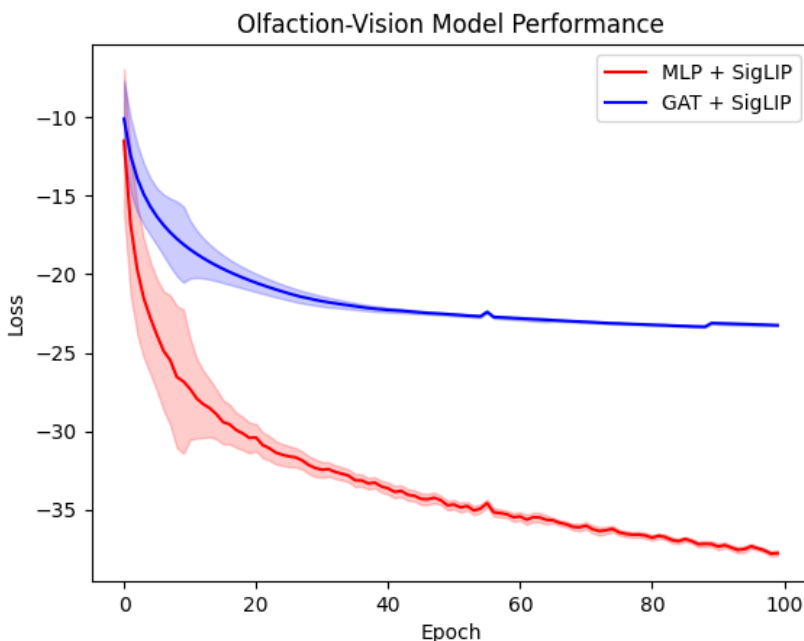


Fig. 10. Training losses for both olfaction-vision models. Note that the GAT-based model is more accurate, but requires more compute and inference time, and thus violates our constraints for full edge computation. As a result, the MLP-based model is used for our final results.

Full code to reproduce the training data and results for both models are found at [39] and [40], respectively.

E. Training of Reinforcement Learning Algorithms

In order to construct any learning algorithm for navigation, we needed to solidify the states for which the UAV could possibly reside and the actions available to it in each state. We deduced that for each of 9 different states, 7 actions were possible: turn slightly left (45°), turn slightly right (45°), turn hard left (90°), turn hard right (90°), surge forward, cast left, or cast right. The 9 states are detailed below in Table VIII.

TABLE VIII
STATE TABLE FOR EACH NAVIGATION AGENT

-	Off-Plume	On-Plume (Low Concentration)	On-Plume (High Concentration)
Left Sensor < Right Sensor	0	3	6
Left Sensor == Right Sensor	1	4	7
Left Sensor > Right Sensor	2	5	8

Two TD(λ) algorithms were selected for simulation as a possible navigation algorithm: Q(λ) and Expected SARSA(λ).

Q-learning is an off-policy temporal-difference (TD) method that directly estimates the optimal action-value function without requiring adherence to the policy used for exploration [33]. It learns a policy that selects state-action transitions yielding the highest reward and is among the most widely adopted TD algorithms in reinforcement learning due to its computational simplicity and its effectiveness in approximating long-term cumulative return.

Greedy Q-learning performs well in settings where rewards are clearly defined for each state. From an intuitive standpoint, an agent that optimizes expected reward is better positioned to approximate the latent reward structure of an environment than an agent that strictly maximizes instantaneous reward, as in standard Q-learning. This distinction becomes particularly relevant in environments characterized by continuous gradients of a target compound. However, complications arise when the environment contains regions devoid of the target signal. During early training, reward assignments in such regions are highly uncertain, causing a Q-learner to maximize an unreliable objective. In contrast, an Expected SARSA learner [41] estimates the expectation over possible actions, thereby approximating the policy itself and effectively reducing loss. Although regularization can partially mitigate this issue, it does not fully resolve the instability introduced by erroneous reward estimates.

In much of contemporary reinforcement learning research - especially in domains with directly observable environments - Q-learning and its variants represent a practical compromise between computational cost and performance. Our experimental results, however, indicate that the effectiveness of Q-learning depends strongly on the agent’s ability to observe rewards that faithfully reflect ground truth. When reward signals are reliable, a greedy Q-learner is likely to achieve superior performance. For this reason, we posit that Expected SARSA constitutes a more robust choice in general, with its update rule given by

$$Q^*(s, a) = Q(s, a) + \alpha \left[R(s, a, s') + \frac{\gamma}{n} \sum_{i=1}^n Q(s'_i, a'_i) - Q(s, a) \right]$$

Expected SARSA further allows for explicit control over the degree of greediness in the policy. As ϵ converges to 1, Sutton and Barto [41] demonstrate that the method converges to selecting the action with maximal cumulative reward, thereby becoming equivalent to Q-learning. This flexibility enables Expected SARSA to combine the benefits of both paradigms by adjusting policy learning according to the reliability of reward estimates and the self-paced learning parameter λ . Accordingly, the early stages of training resemble SARSA,

$$Q^*(s, a) = Q(s, a) + \alpha [R(s, a, s') + \gamma Q(s', a') - Q(s, a)]$$

which dampens excessive loss, and gradually transition toward Q-learning, moderating the high loss, and then evolve into Q-learning

$$Q^*(s, a) = Q(s, a) + \alpha \left[R(s, a, s') + \gamma \max_{a'} Q(s', a') - Q(s, a) \right]$$

as the policy improves. This formulation allows the algorithm to operate in both on-policy and off-policy regimes.

A closer inspection reveals that the principal distinction between Expected SARSA and Q-learning lies in replacing reward maximization with reward averaging. Consequently, Expected SARSA incurs greater computational cost, since an expectation over actions must be evaluated at each update. Nevertheless, this added expense yields increased robustness and accuracy during co-training by reducing the volatility associated with early reward mis-estimation. This advantage is particularly pronounced in the initial phases of learning, when unrewarded trajectories may be assigned highly inaccurate values due to frequent blank observations. Because the objective is to infer rewards for unobservable states with greater fidelity, the additional computational burden may be warranted. Expected SARSA thus provides a principled mechanism for interpolating between on-policy and off-policy learning while offering an inherent means of controlling reward loss. In our experiments, ϵ in Expected SARSA is permitted to increase as a function of the self-paced learning parameter.

In light of the above, simulation showed that Expected SARSA(λ) was more robust to perturbations in the environment, reasoning about blanks, and training parameter changes, so it was selected as the finalist to deploy onto the UAV for evaluation. Both algorithms were trained with the following configuration: Details on its architecture are shown below:

The training losses for the final configurations of both algorithms can be found in Tables 11 and 12. Table 11 shows how Q(λ) performs better in a simulation when no blanks are modeled. In other words, there are no spots within the navigation environment that are absent of the target compound. In reality, this is not probable, and it is prudent to model "blanks" of pockets of air that contain virtually no trace of the target compound [31]. Note the tighter variance bands around Q(λ) toward the end of training for the simulation modeled without blanks.

When we model blanks in the environment, Expected SARSA(λ) out-performs Q(λ). We expect that this is due to Expected SARSA being more robust to noise than greedy Q-learning as noted by [34], [42], [43].

TABLE IX
 $Q(\lambda)$ & EXPECTED SARSA(λ) CONFIGURATION

Parameter	Value
number of states	9
number of actions	7
episodes	10000
γ (discount factor)	0.9
α (learning rate)	1e-4
ϵ (greediness)	1.0
ϵ -decay	0.999
λ (TD step size)	0.8

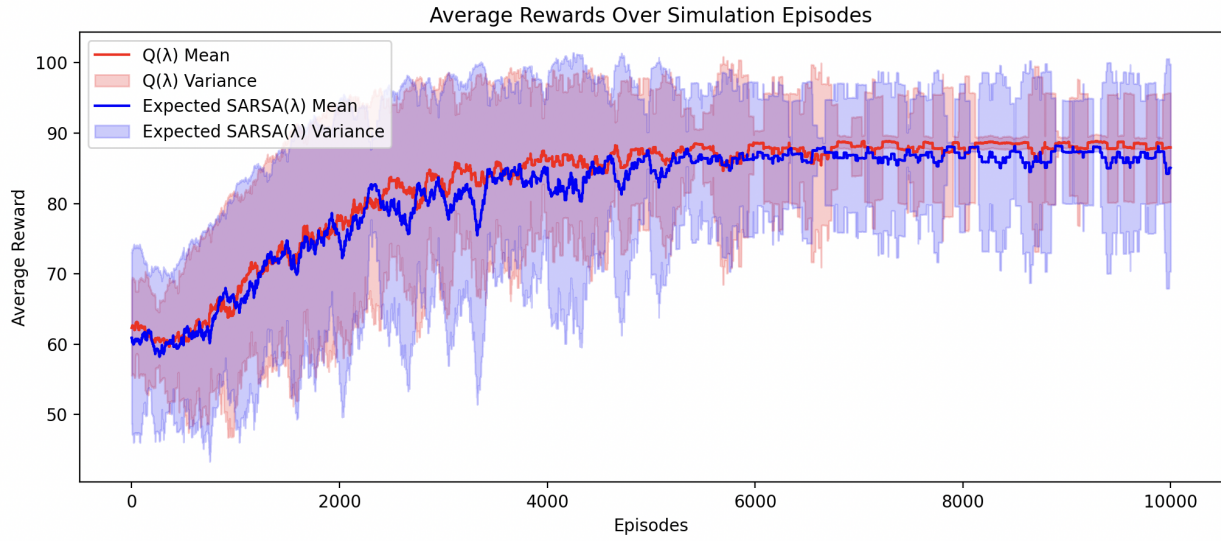


Fig. 11. Training losses for both $Q(\lambda)$ and Expected SARSA(λ) algorithms with no blanks modeled.

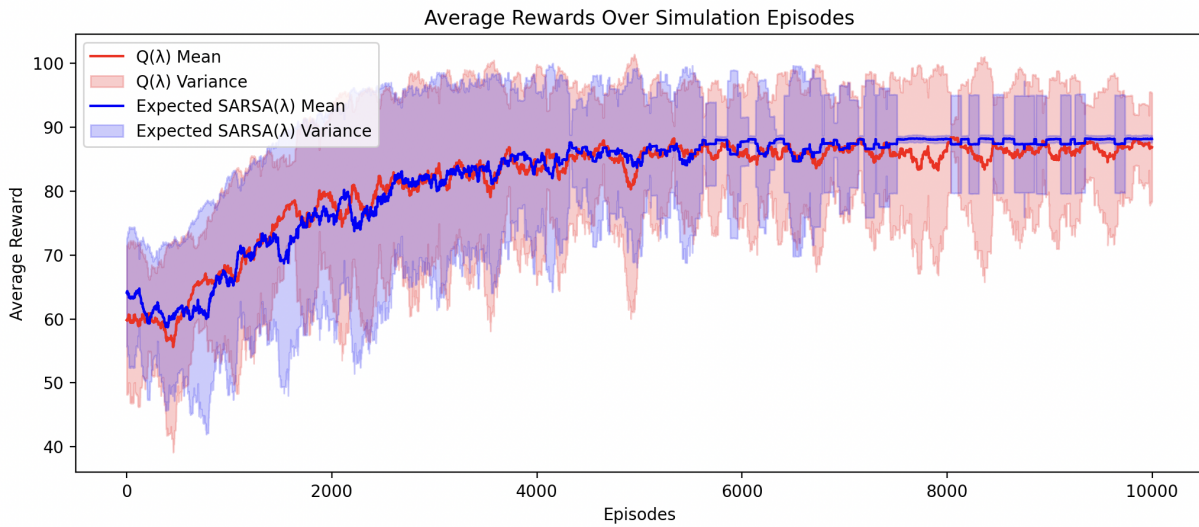


Fig. 12. Training losses for both $Q(\lambda)$ and Expected SARSA(λ) algorithms with blanks modeled.

At the conclusion of training, a Q -value table is created showing credit assignment to each action. The final Q -values for the final policy can be found in Figure 13 below.

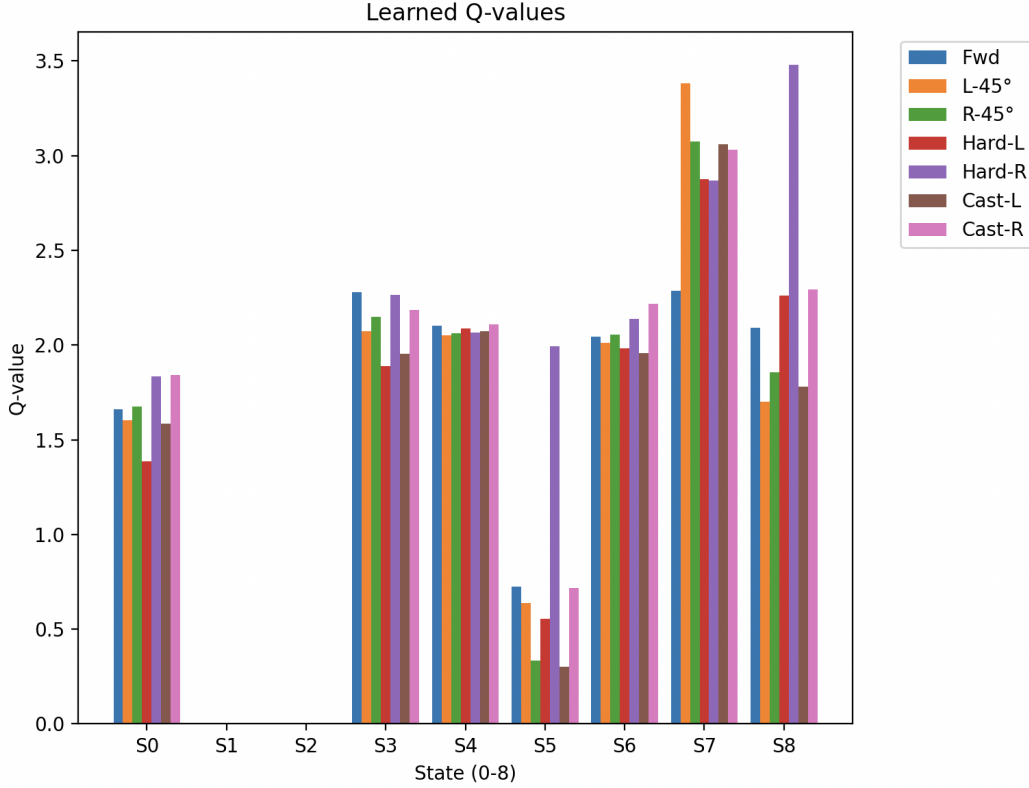


Fig. 13. Q -values of the final reinforcement learning policy.

F. Plume Model Environment

A plume environment was built to understand behavioral dynamics of gases over time. The environment was used as a model to evaluate the effects on air volatility from changing different parameters. It was later used to help model navigation algorithms for the UAV. The environment was built on top of the *Gymnasium* framework and is included within the code repository associated with this paper.

We note the configuration to reproduce our results below.

TABLE X
PLUME ENVIRONMENT PARAMETERS

Parameter	Value	Units	Description
Diffusion	1.0	Dimensionless	Rate of gas dispersion per timestep; conditional on compound
Sparsity	0.0	Dimensionless	Useful for modeling blanks over long distances; conditional on compound
Temperature	20.0	Degrees Celsius	Assume constant air temperature due to short durations and distances
Relative Humidity	50.0	Percentage	Assume constant relative humidity due to short durations and distances
Air Density	1.225	kg/m^3	Assume constant air density due to short durations and distances
Wind Speed	1.0	m/s	Average windspeed along x -direction
Emission Rate	1.0	kg/s	Rate of gas emission from source; conditional on compound
Pasquill Stability	D	Class A-G	General air volatility characteristic; conditional on compound
Source Height	1.0	m	Maximum of 3.0 meters was modeled due to flight envelope of UAV
Obstacles	5	Integer count	Only square block obstacles are modeled

G. Olfaction Sensor Breakout Board

There are several different olfaction sensors that exist. In order for us to understand which ones were best suited for the detection of ethanol, we designed a breakout board that assessed several olfaction sensors in parallel. Responses to concentration changes in ethanol were documented and compared, leading to the ultimate selection of the metal oxide and electrochemical sensors as the best fit for tracking ethanol. The electrical schematics and Gerber files for this circuit board are available in

the code repository associated with this paper in order to encourage olfactory research. Figure 14 shows the final assembled breakout board. Figure 15 shows the electrical schematic of the board. Data for assessing maximum sensor response was accumulated with this board via the *Scientece* olfactory interface application [44].

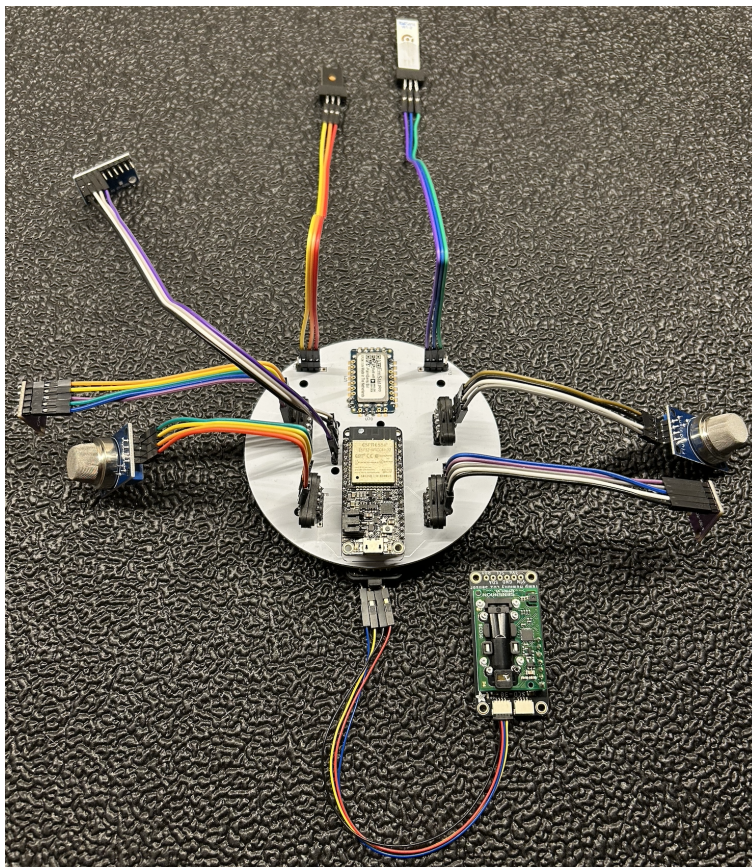


Fig. 14. An image of the breakout board designed to down-select the olfaction sensors for ethanol detection.

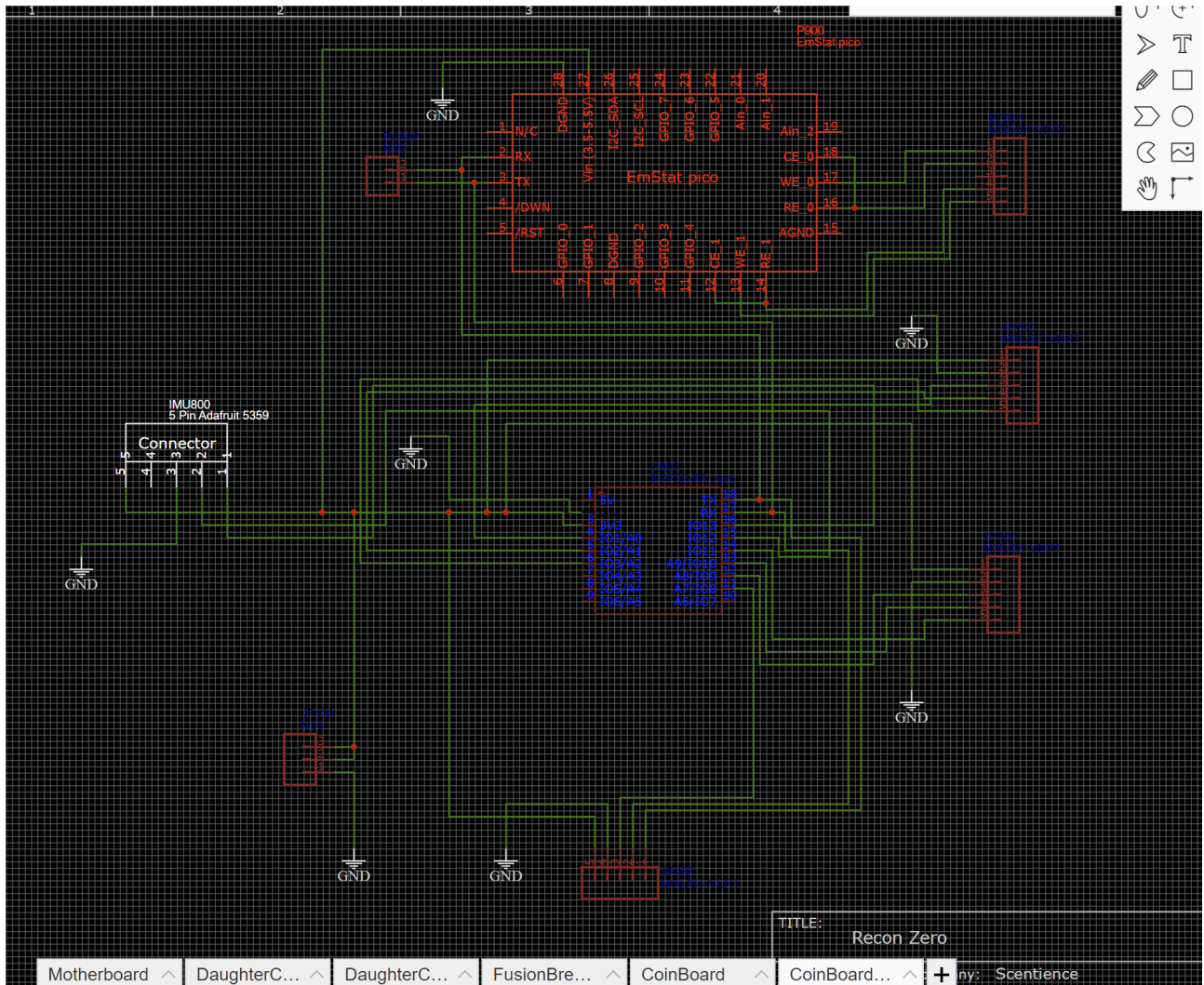


Fig. 15. Electrical schematic of the breakout board above. Gerber files and full schematics for this board are provided in the code repository associated with this manuscript.

H. Mechanical Modifications to the UAV

To adapt the UAV for olfactory navigation, we designed a mechanical harness that equipped the machine with the OPU, olfaction sensors, battery, ballast, and infrared sensors. All components were designed in SolidWorks and iterated several times; the final iterations are located in the code repository under the */cad* subdirectory. Generally-accepted mechanical design principles for aeronautics were followed. The full kit can be 3D-printed on a single 500mm x 500mm print bed using PLA plastic. We used a 35% infill to balance durability and weight. A full bill of materials can be found in the code repository.

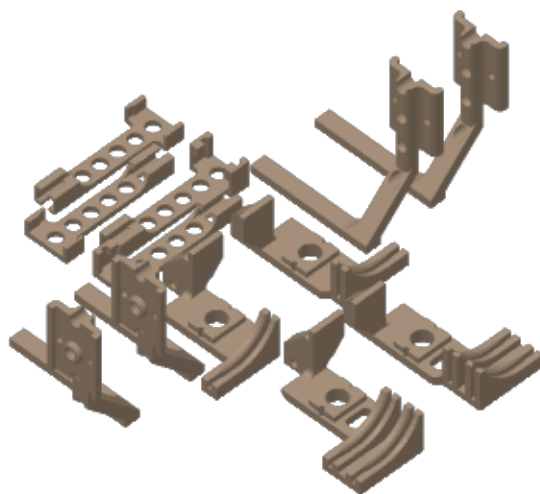


Fig. 16. The full UAV modification kit for both electrochemical and metal oxide sensing configurations can be additively manufactured on a single 200mm x 200mm print bed.